Resonant magneto–optical Kerr effect induced by hybrid plasma modes in ferromagnetic nanovoids*

Xia Zhang(张霞)[1,†], Lei Shi(石磊)[2], Jing Li(李晶)[3], Yun-Jie Xia(夏云杰)[1], and Shi-Ming Zhou(周仕明)[4]

[1] *Shandong Province Key Lab of Laser Polarization and Information, Qufu Normal University, Qufu* 273165, *China*
[2] *Surface Physics State Laboratory and Department of Physics, Fudan University, Shanghai* 200433, *China*
[3] *Department of Optical Science and Engineering, Fudan University, Shanghai* 200433, *China*
[4] *Department of Physics, Tongji University, Shanghai* 200092, *China*

(Received 22 March 2017; revised manuscript received 16 August 2017; published online 29 September 2017)

With nanovoids buried in Co films, resonant structures were observed in spectra of polar magneto–optical Kerr effect (MOKE), where both a narrow bandwidth and high intensity were acquired. Through changing the thickness of Co films and the lattice of voids, different optical modes were introduced. For a very shallow array of voids, the resonant MOKE was induced by Ag plasma edge resonance, for deeper ones, hybrid plasma modes, such as void plasmons in the voids, surface lattice plasmons between the voids, and the co-action of them, etc. resulted in resonant MOKE. We found that resonant MOKE resulted from the void plasmons resonance which possesses the narrowest bandwidth for the lowest absorption of voids. The simulated electromagnetic field (EF) distribution consolidated different effects of these three optical modes on resonant MOKE modulation. Such resonant polar MOKE possesses high sensitivity, which might pave the way to on-chip MO devices.

Keywords: magneto–optical Kerr effect, surface plasma polariton, nanocavity mode, surface lattice resonance

PACS: 78.20.Ls, 73.20.Mf, 75.70.–i **DOI:** 10.1088/1674-1056/26/11/117801

1. Introduction

Engineering the interplay between magnetic fields and plasmons is very important both in telecommunication and integrated optical devices.[1–3] This topic includes two aspects, one is actively controlling surface plasma plamons (SPP) by an external magnetic field,[4–8] and the other is magnetic properties of ferromagnetic materials modulated by SPP.[9–13] The magneto–optical Kerr effect (MOKE), as a polarization based technique, possesses high sensitivity and may be used in characterizing the interplay of magnetic fields and plasmons.[14] Meanwhile, the interaction between surface plasmons and the magnetic fields may facilitate the MOKE modulation,[15] which promotes the usage of MOKE in magneto–optical devices and basic physics research.

Owing to the emergency of magnetic plasma waves,[16] large and resonant MOKEs have been found in bounded electrons.[17–19] The physical mechanism was microscopically elucidated by the introduction of the cyclotrons frequency, which combined with plasma edge resonance of bulk metals led to large and resonant MOKEs. In the macroscopic view, these effects are attributed to the complex effective refraction index approximated to that of the measurement circumstances.[20] In general, MOKEs modulated by plasma edge resonance are limited to the intrinsic properties of materials. With the development of nanofabrication techniques, surface plasma plasmons can be manipulated arbitrarily.[21–23] Plasma enhanced MOKEs are attracting more and more attention both in optical and magnetic areas,[9–13,24–26] nowadays. In Co_xAg_{1-x} core-shell nanoparticles,[27,28] an enhanced magneto–optical Kerr effect (MOKE) is acquired by the localized SPP, and the peak in polar MOKE spectrum has been modulated by both nanoparticle size and composition.[28] MO activity enhanced by localized SPP was also found in Au/Co/Au-sandwiched two-dimensional (2D) systems, with both ordered and random Au nanostructures decorated on Co/Au films, modulated polar MOKEs were presented, and the location of peaks in polar MOKE spectra depends on the size of Au nanoparticles.[29,30] In sandwiched 2D planar photonic crystals, with an external magnetic field applied along with the wavevector of light and in the plane of the sample, both localized and propagated SPP modes were excited which resulted in enhanced transverse MOKEs.[31,32] All the above are related to the nanostructured noble metal decorated on ferromagnetic films. Besides, modulated MO effects have been demonstrated in magneto–plasmonic metamaterials,[33–35] hybrid plasmonic metasurfaces,[36,37] coupled resonators,[38,39] topological insulators,[40–42] 2D materials,[43–45] etc. Magnetic-free MO effects were proposed,[36–38] which may pave the way to on-chip magneto–optical devices.

However, in nanostructured ferromagnetic arrays, besides the size, shape, and the arrangement of nanoparticles or holes,

*Project supported by the Natural Science Foundation of Shandong Province, China (Grant No. ZR2015AM024) and the Doctoral Research Started Funding of Qufu Normal University, China (Grant No. BSQD20130152).

†Corresponding author. E-mail: xzhangqf@mail.qfnu.edu.cn

© 2017 Chinese Physical Society and IOP Publishing Ltd

the altered gyroelectric nanostructured ferromagnetic materials at optical frequency have provided plenty of intriguing scientific wealth.[46,47] It has been reported that additional optical modes had been introduced through the surface lattice plasmons scattered by the nanomagnets.[48–50] By tuning the phase of localized SPP in the two orthogonal directions, MOKEs were modulated due to the two orthogonal damped oscillators coupled through spin–orbit interaction.[51] In 2D magnetic nanoparticle arrays, Fano-type profile has been revealed in the MOKE spectrum due to the coupling between surface lattice plasmons that occurred in the orthogonal directions.[52,53]

The modulated MOKE signal of ferromagnetic films through PSS array caped have been studied in our former work,[54–57] where the PSS array, as two-dimensional gratings, plays a key role in surface mode occurrence. Whereas in Co/Pt nanocaps fabricated on the PSS array template, MOKEs are modulated by SPP and Mie scattering optical modes.[58]

Different from the former work above, in this paper, by using 2D polystyrene spheres (PSS) as template, combination nanosphere lithography (NSL) with ferromagnetic film electrochemical deposition, two series samples of glass/Cr/Ag/Co nanostructured ferromagnetic were fabricated. In series 1 (S1), we fixed the lattice and varied depth of the voids by changing the deposition time, and in series 2 (S2), we fixed the deposition time and varied the lattice of voids by changing the PSS diameter. Different from our former work where multiple peaks and dips occurred in the spectra, the MOKE spectra of Co nanovoids demonstrated one dominated resonant configuration, which possessed a narrow bandwidth and a high MOKE signal. The physical mechanisms were elucidated through the analysis of electromagnetic field (EF) distribution calculated by commercial FDTD solution software.

2. MOKE theory in 2D magnetic photonic crystal (MPC) slabs

Under an external magnetic field applied perpendicular to the electric field of light ($M \perp E$), the degenerate eigenstates of light can split into right circularly and left circularly polarized (RCP and LCP) states. For most materials, the refraction indices of RCP and LCP light are different, and this difference is the origin of magneto–optical (MO) effects in macroscopic aspect.[14,59] Polar magneto–optical Kerr effect (MOKE) is given as[14]

$$\Phi_k = \theta_k - \mathrm{i}\varepsilon_k, \tag{1}$$

where θ_k is the Kerr rotation and ε_k is the Kerr ellipticity. For the microscopic analysis, the MOKE signal is related to the conductivity from the Fresnel equation, and the formula of Kerr rotation (θ_k) is given as[14,20]

$$\theta_k = \mathrm{Re}\left(\frac{\tilde{\varepsilon}_{xy}}{\mathrm{i}\,(\tilde{\varepsilon}_{xx}-1)\sqrt{\tilde{\varepsilon}_{xx}}}\right). \tag{2}$$

Obviously, at optical frequency, the gyrotropic properties of ferromagnetic properties are mainly dependent on the grotroelectric mechanism. As is well known, under an external magnetic field, the permittivity is a tensor as[14]

$$\widehat{\varepsilon} = \begin{pmatrix} \varepsilon_{xx} & \mathrm{i}\varepsilon_{xy} & 0 \\ -\mathrm{i}\varepsilon_{xy} & \varepsilon_{yy} & 0 \\ 0 & 0 & \varepsilon_{zz} \end{pmatrix}, \tag{3}$$

where $\tilde{\varepsilon}_{xx}$ and $\tilde{\varepsilon}_{xy}$ are the diagonal and off-diagonal components of the dielectric permittivity tensor, respectively. The off-diagonal part $\tilde{\varepsilon}_{xy}$ is related to the net magnetization of materials and comes from the spin activities of electrons in ferromagnetic materials, which is proportional to the gyrotropic parameter of ferromagnetic materials.[59] The diagonal part $\tilde{\varepsilon}_{xx}$ denotes the optical properties of materials and can be manipulated by the aid of a nano-fabrication technique easily, nowadays.

In a 2D MPC slab, when light propagates along the in-plane direction, plasmas would experience multiple Bragg scatterings due to the introduced periodicity of the 2D MPC, and the following momentum match condition could be satisfied with the assistance of 2D periodic structure:[54]

$$\boldsymbol{K} = \boldsymbol{K}_0 \pm \boldsymbol{G}_x \pm \boldsymbol{G}_y, \tag{4}$$

where the in-plane momentum of the incident light $\boldsymbol{K}_0 = 2\pi/\lambda \sin\theta$ with an incidence angle θ, $\boldsymbol{G}_x$, and $\boldsymbol{G}_y$ present the reciprocal lattices of 2D MPC in two primitive axes. The refraction vector is proportional to the wave vector as

$$\boldsymbol{n} = (c/\omega)\,\boldsymbol{K}, \tag{5}$$

which denotes the modulated optical property by different optical modes. In general, this modulation is mainly related to the diagonal parts of the dielectric permittivity.

Obviously, MOKE in 2D MPC is modulated not only by the field intensity but also through the alteration of permittivity. From Eq. (3), we can deduce that the Kerr rotation θ_k can become tremendous if $\sqrt{\tilde{\varepsilon}_{xx}} \to 1$. With PSS arrayed on the ferromagnetic films, the effective permittivity $\tilde{\varepsilon}_{xx}$ has been manipulated through introducing surface modes and demonstrating the enhanced MOKE of Fe film.[54–57]

Here, in 2D nanostructured ferromagnetic voids, besides surface lattice resonance modes, the noble metal substrate effects and nanocavity modes have been manipulated by controlling the depth of the voids. From the Lorentz line shape analysis of θ_k and ε_k according to Eq. (1), resonant MOKE is revealed due to the hybrids optical modes introduced.

3. Sample fabrication and study

Co nano-voids were fabricated on glass using NSL combined with electrochemical deposition; the fabrication steps are displayed in Fig. 1(a). Firstly, Cr (20 nm)/Ag (200 nm) films were prepared on glass by two-source dc magnetron

sputtering from Cr and Ag targets. Here, Cr (20 nm) was deposited as the buffer before Ag to strengthen the adhesion of Ag. The templates of glass (substrate)/Cr (20 nm)/Ag (200 nm)/PSS were synthesized in step 2 (for the details, please refer to Ref. [56]). In step 3, Co films were deposited into the interstices of PS sphere templates formed in step 2 from Co aqueous electrolyte by electrochemical deposition, where a three-electrode method was performed, the templates were used as the working electrode, Pt wire as the counter electrode, and Ag/AgCl as the reference electrode. In the last step, the PSSs were dissolved in the tetrahydrofuran and acetone by sonication for 30 min at temperature below 30 °C alternately, and thus Co nanovoids were formed on Ag substrate. To avoid the ferromagnetic material oxidation, 3 nm SiO_2 films were deposited on the nanovoids by electron beam evaporation. Samples S1 were fabricated with a fixed PS diameter $D = 440$ nm and varied deposition time $t = 20$, 60, 100, and 150 s according to the cyclic voltammetry (CV) as shown in Fig. 2(a). Samples S2 were fabricated on the template with a fixed deposition time $t = 150$ s and different template lattices $a = 530$, 620, 760 nm. For comparison, Co film deposited on the unpatterned glass/Cr/Ag was also carried out with $t = 150$ s. All electrochemical depositions were carried out at the working electrode with potential $U = -1$ V.

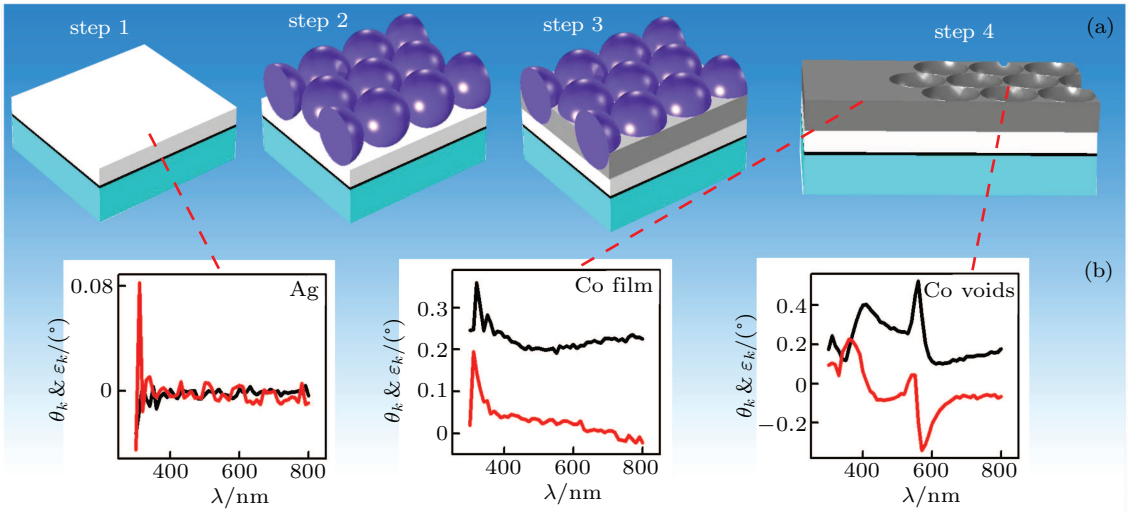


Fig. 1. (color online) (a) The sample fabrication course, and (b) polar magneto–optical Kerr effect of Ag film (the left), unpatterned Ag/Co film (the medium), and Co nano-voids on Ag film (the right).

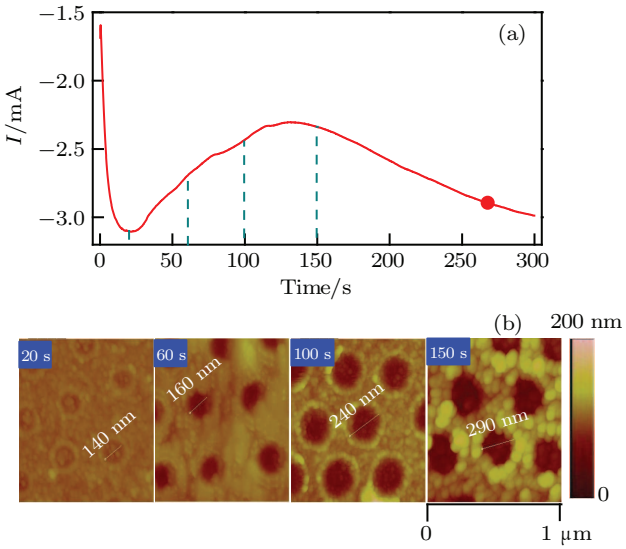


Fig. 2. (color online) (a) Cyclic voltammetry curve at the working electrode, under potential volt $U = -1$ V. (b) Top-view of AFM images of samples with deposition time denoted as the dashed dark green line in panel (a).

The morphologies of all samples were characterized by a commercial atomic force microscopy (AFM) (Slover P47, NT-MDT). Figure 2(b) shows morphologies of samples S1 with different deposition time denoted as the dashed dark green lines in Fig. 2(a). It can be seen that the voids are deepened, and the depths measured by AFM are about 13, 35, 48, and 85 nm or so for $t = 20$, 60, 100, and 150 s, respectively. The outmost diameter increases, which is indicated as the white words in the AFM images.

Polar magneto–optical Kerr rotation θ_k and ellipticity ε_k and optical reflectance R spectra were measured at room temperature by a home-made Kerr spectrometer from 300 nm to 800 nm and a reflectometer from 200 nm to 1200 nm, respectively.[54] Both θ_k and ε_k measurements were carried out with an incident angle of 5° under an external magnetic field of 1.0 T. In the reflectivity measurements, the data were normalized with respect to that of Al films.

Figures 3(a)–3(d) show the measured polar Kerr rotation θ_k (black lines) and ellipticity ε_k (red lines) versus wavelength λ of samples S1 with $t = 20$, 60, 100, and 150 s, respectively. One resonance-like shape is displayed in θ_k and ellipticity ε_k spectra of the sample with deposition time $t = 20$ s (Fig. 3(a)),

which centers at $\lambda = 325$ nm and is right located at the energy of the Ag plasma edge, furthermore, the bandwidth in the θ_k spectrum is narrower than 15 nm. The physical mechanism of this resonant PMOKE is obviously attributed to the bulk Ag plasma edge resonance. It has been reported that PMOKE of bulk Ag displays strong dispersion in the neighborhood of 3.85 eV,[60] whereas the resonant-like shape has not been found in the PMOKE of pure Ag film as can been seen in the leftmost image in Fig. 1(b).

When covered with shallow Co nanovoids, the narrow and resonant MOKE was demonstrated as shown in Fig. 3(a). With the increase of the deposition time $t = 60$ and 100 s, as indicated in Figs. 3(b) and 3(c), the MOKE spectra become broader and red-shift away from the Ag plasma edge. The AFM measurements reveal that the void depths of these two samples are 32 and 48 nm, respectively. The thickness of Co films more than 20 nm surpasses the skin depth,[61] therefore, the impact of Ag plasma edge on PMOKE becomes weak. When deposition time $t = 150$ s, one broad resonant structure occurs at the wavelength $\lambda = 412$ nm, near the location of the lattice with $a = 440$ nm, as indicated in Fig. 3(d), which is different from MOKE signals of both Ag film and Co/Ag film denoted as the leftmost and middle images in Fig. 1(b). The phenomenal explanation can be referred to that more electromagnetic field is localized in the deepened voids, so called void plasmons occurred, which can be regarded as dipole oscillators.[62,63] The diffractive coupling of these oscillated dipoles results in surface lattice plasma resonance, and the resonant PMOKE spectra in Fig. 3(d) resemble that of dipole oscillator resonance.[64]Besides, Ag plasma edge induced resonant structure occurs at $\lambda = 323$ nm, and this can be attributed to that surface plasma plasmons induced extraordinary optical transmission (EOT) surpasses the limits of the skin depth effect.[65]

The reflection spectra of samples S1 are shown in Figs. 3(e)–3(h). The blue dashed line in Fig. 3(e) is the absorption index of bulk Ag, and that in Fig. 3(h) is the reflection spectrum of Co film deposited on Ag with time $t = 150$ s. Obviously, the reflection dips correspond to λ or ε_k peaks well. In Fig. 3(e), the spectrum of absorption index (the blue dashed line) is fully coincident with that of the sample with $a = 440$ nm and $t = 20$ s (the solid black lines), which validates the origin of the MOKE signal of the sample with deposition time $t = 20$ s as the noble metal substrate effect.[20] The dips in the other three reflection spectra in Figs. 3(f)–3(h) located at wavelength $\lambda = 332$, 334, 414 nm corresponding to ε_k peaks in Figs. 3(b) and 3(c), and to the ε_k dip in Fig. 3(d). In the reflection spectrum of unpatterned Co film deposited on Ag at $U = -1$ V and $t = 150$ s (Fig. 3(h) the blue dashed line), a shallow valley located at $\lambda = 402$ nm can be discerned, which is ascribed to surface plasma plasmons (SPPs) at the interface of Ag/Co films. Moreover, it is adjacent to the dip located at 414 nm in the solid purple line. From above, we deduce that the peak at $\lambda = 414$ nm in the PMOKE spectrum in Fig. 3(d) of the sample with deposition time $t = 150$ s originates from combined effects of localized void plasmons and surface lattice plasmons, and the bandwidth is broadened due to the high absorption of Co.

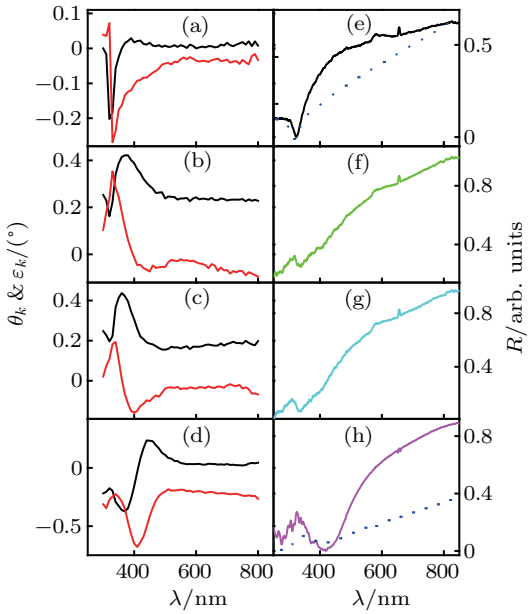


Fig. 3. (color online) θ_k (black lines) and ε_k (red lines) (a)–(d), and reflection spectra (e)–(h) as a function of λ of sample S1 with deposition time $t = 20$, 60, 100, and 150 s from up to down. The blue dashed lines in panels (e) and (h) are the extinction spectrum of Ag and the reflection spectrum of Co film on Ag with deposition time $t = 150$ s.

Surface lattice plasmons modulated resonant polar MOKE can be manipulated by varying lattice. Figure 4 shows the MOKE (Figs. 4(a)–4(c)) and reflection (Figs. 4(d)–4(f)) spectra versus wavelength λ of samples S2 with fixed deposition time $t = 150$ s and varied diameters of PS sphere as $a = 530$, 620, and 760 nm, respectively. The corresponding morphology images of samples S2 are also given in the leftmost images in Fig. 4, where the depths $h = 170$, 120, 126 nm are denoted as oscillation in right-down insets, and the outmost diameter of the voids $d = 480$, 490, 460 nm could be achieved by AFM for samples with lattices a= 530, 620, 760 nm from up to down.

Obviously, weak Ag plasma edge resonance induced polar MOKE at $\lambda = 325$ nm is still observed in θ_k and ε_k spectra (Figs. 4(a)–4(c)) of all samples as indicated by the dashed vertical purple line. Besides, two other pronounced structures dominate θ_k and ε_k spectra of all samples. For clarification, the orders of all θ_k peaks are marked. The wavelength of broad ones R1 are almost fixed around $\lambda = 402$ nm for all three samples as denoted by the dashed vertical dark green lines, which can be ascribed to SPP at the interface of Co–Ag films, as that in Fig. 3(d) (the blue dashed line). Other than fixed peak R1, the strong resonant ones R2 vary with the increase

of the PS sphere diameter, which locate near $\lambda = 480$, 551, and 682 nm for samples with $a = 530$, 620, 760 nm, respectively. Polar MOKE is modulated and enhanced at peaks R2 for samples S2. While, the polar MOKE spectra at the location of R2 peaks in Figs. 4(a)–4(c) demonstrate different peculiarities. The half-bandwidth of θ_k peaks R2 broadens with the increase of the lattice a. The θ_k spectrum in Fig. 4(a) demonstrates the narrowest resonance located near $\lambda = 480$ nm, which corresponds well to the diameter of nanovoids, and it can be attributed to void plasmon resonance, and low loss of the nanovoids leads to the narrowest polar MOKE signal. The wavelength locations of the resonant structures for the other two (Figs. 4(b) and 4(c)) are larger than the diameter of the nanovoids (Figs. 4(m) and 4(n)) and nearer to the lattice, here, we ascribe them to combined effects of void plasmons and surface lattice resonances, which have been found in samples S1 with deposition time $t = 150$ s as denoted in Fig. 3(d).

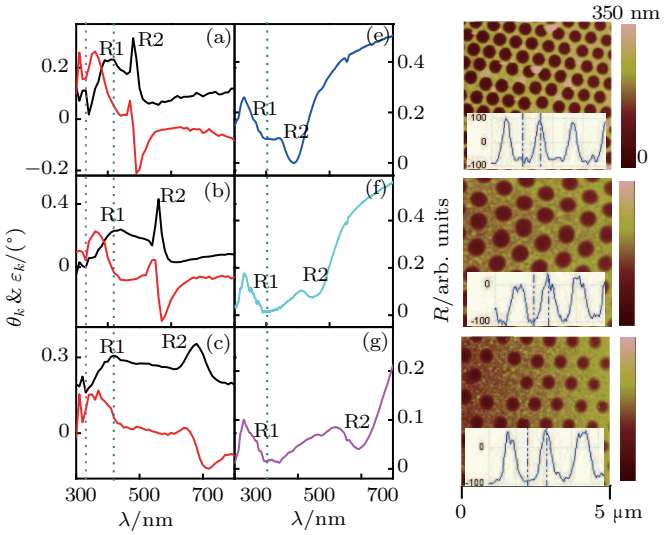


Fig. 4. (color online) θ_k (black lines) and ε_k (red lines) (a)–(c) and reflection (d)–(f) spectra as a function of λ for samples S2. The leftmost column is the top-view AFM images of samples S2. Both the spectra and images are for samples with $a = 530$, 620, and 760 nm from up to down, respectively.

The dips of reflection spectra versus wavelength λ in Figs. 4(d)–4(f) show similar variation trends as peaks of θ_k spectra in Figs. 4(a)–4(c). The marked shallow dips R1 of all samples are fixed around $\lambda = 401$ nm, which correspond to R1 peaks in the θ_k spectra. R2 minima vary with the increase of the lattice a, for samples with $a = 530$, 620, 760 nm, the wavelength of R2 minima are located around $\lambda = 480$, 557, and 692 nm, respectively. One can find that the deep reflection valleys R2 right correspond to the strong θ_k peaks R2, except for that of the sample with lattice $a = 760$ nm, where the R2 dip deviates slightly from θ_k peaks but tends to ε_k dip. In case of samples with $a = 530$ nm, the wavelength of the R2 location (Fig. 4(d)) is nearer to the outermost diameter of voids, and thus the R2 resonance can be mainly attributed to void plasmon resonance, where the low loss of voids results in the narrowest resonant polar MOKE at R2 location (Fig. 4(a)). Whereas for that of samples with $d = 620$, and 760 nm (Figs. 4(e) and 4(f)), the wavelength of R2 is nearer to lattice a, as that in the polar MOKE spectrum of the sample with deposition time $t = 150$ s and diameter $d = 440$ nm. The line shapes of resonances induced by purely void plasmons are narrower in spectrum Fig. 4(a) than that induced by combined effects of void plasmons and surface lattice plasmons in spectra Figs. 4(b), 4(c), and 3(d). It is comprehensible that the absorption of air is much lower than that of ferromagnetic Co films.

Above we only phenomenally discussed the resonant PMOKE induced by different optical modes such as bulk Ag plasma, nanovoid plasmons, surface lattice plasmons resonance, or their combined effects. To determine the physical mechanism, the electromagnetic field (EF) distribution for all samples under far-field p-polarized excitation (with E-field along the x-direction) and near-field detection (with the detector placed in the middle of the voids) were performed using the finite-difference time-domain (FDTD) method (commercial lumerical solutions). The parameters of Co and Ag are measured using ellipsometry. The meshes divided at nanovoids are 1 nm in the simulation.

In Fig. 5, we provide the simulated results of samples S1. Firstly, both the calculated (the light green lines) and the measured reflectivity spectra (the black lines) are shown in Figs. 5(a)–5(d), it is obvious that they agree well with each other, in particular with respect to reflectivity minima in the spectra, which consolidate our material research base and method reliability. The corresponded EF distributions of these reflectivity minima are displayed both in the xy-plane (Figs. 5(e)–5(h)) and the xz-plane (Figs. 5(i)–5(l)) for samples with deposition time $t = 20$ s (Figs. 5(e) and 5(i)), 60 s (Figs. 5(f) and 5(j)), 100 s (Figs. 5(g) and 5(k)), and 150 s (Figs. 5(h) and 5(l)), respectively. It is noticeable that EFs in the xy-plane in Figs. 5(e)–5(h) reveal gradually enhanced void plasmons with more and more EFs distributed in the voids with the increase of the deposition time from 20 s to 150 s. The EF for the sample with $t = 20$ s in Fig. 5(e) at minimum $\lambda = 325$ nm is almost uniform apart from some hardly discerned sparkles in the shallow voids, whereas the EF distribution at $\lambda = 414$ nm for the sample with $t = 150$ s in Fig. 5(h) is highly centralized in the voids and jointed with the adjacent ones. The EFs in the xz-plane in Figs. 5(i)–5(l) demonstrate the similar tendency, for the shallow voids with $t = 20$ s in Fig. 5(i), the EF is distributed at the Ag-voids interface, and with increased deposition time, the voids deepen and widen, and the EF is mainly distributed in the voids.

From the EF distributions both in the *xy*-plane and *xz*-plane of minima in spectra Figs. 3(e)–3(h), we could confirm their origin of resonant MOKE. For shallow voids buried in thin Co film, as the sample with deposition time $t = 20$ s, resonant MOKE in Fig. 3(a) occurs due to the bulk Ag plasma edge resonance, but for the deeper one as deposition time $t = 150$ s, the combined effects of void plasmons and surface lattice plasmons resonance result in the resonant MOKE in Fig. 3(d).

The EF distributions of reflectivity minima R2 (Figs. 4(e)–4(g)) of samples S2 are shown in Fig. 6. Clearly, in Fig. 6(a) for the sample with lattice $a = 530$ nm, the EF distribution of dip R2 in the *xy*-plane is almost all concentrated in the voids, whereas between the voids, it is uniform and nearly zero. But for the other two samples, the EF distributions of dips R2 in the *xy*-plane in Figs. 6(b) (for the sample with $a = 620$ nm) and 6(c) (for the sample with $a = 760$ nm) demonstrate both strong localization in the voids and weak propagation between the voids. The EF distributions of dips R2 in the *xz*-plane in Figs. 6(d)–6(f) reveal the EF distributions in the voids. For the sample with lattice $a = 530$ nm in Fig. 6(d), the EF of the dip located at $\lambda = 480$ nm is mainly distributed at the interface of Co-air and circled around the voids as denoted by slits between two dashed dark green lines. Thus, the voids can be regarded as nanocavities, and the R2 peak of resonant MOKE in Fig. 4(a) can be attributed to the optical mode of cavity resnoance. However, for the other two samples with $a = 620$ and 740 nm, besides the void plasmons, the EF distributions in the *xz*-plane at dips with $\lambda = 557$ nm and $\lambda = 692$ nm demonstrate rim plasmons denoted as purple dashed lines, where the EF surpasses the nanocavity slit, denoted as dashed dark green lines in Figs. 6(e) and 6(f), respectively.

For the sample with $a = 530$ nm, the mechanism of resonant PMOKE can be attributed to the void plasmons,[62] where more EF distributes (Figs. 6(a) and 6(d)) in the voids, and lower loss of the voids results in the narrower θ_k peaks in Fig. 4(a). The EF distributions of dips R2 of samples $a = 620$ (Figs. 6(b) and 6(e)) and 760 nm (Figs. 6(c) and 6(f)) reveal the same mechanism of combined effects of the surface lattice and void plasmons resonance as that of sample $a = 440$ nm in Fig. 2(d), the higher absorption of Co leads to the broader bandwidth in Figs. 4(b) and 4(c). The EF distributions of dips R2 of samples S2 are obviously in accordance with the spectra analysis, which consolidates the physical mechanism of resonant PMOKE.

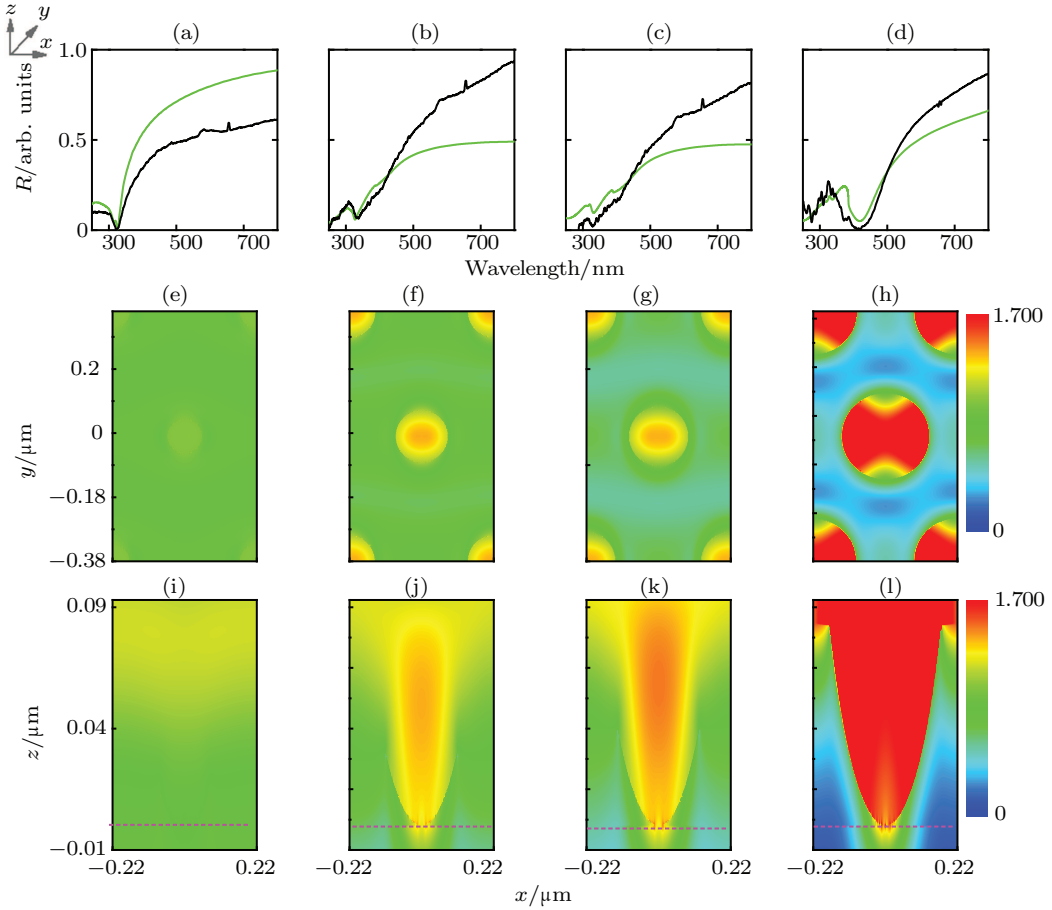


Fig. 5. (color online) (a)–(d) Measured (black lines) and simulated (green lines) reflection spectra versus λ of samples S1, (e)–(h) field amplitude distributions in *xy*-plane, (i)–(l) field amplitude distributions in the *xz*-plane. The dashed lines denote the Ag-voids interface.

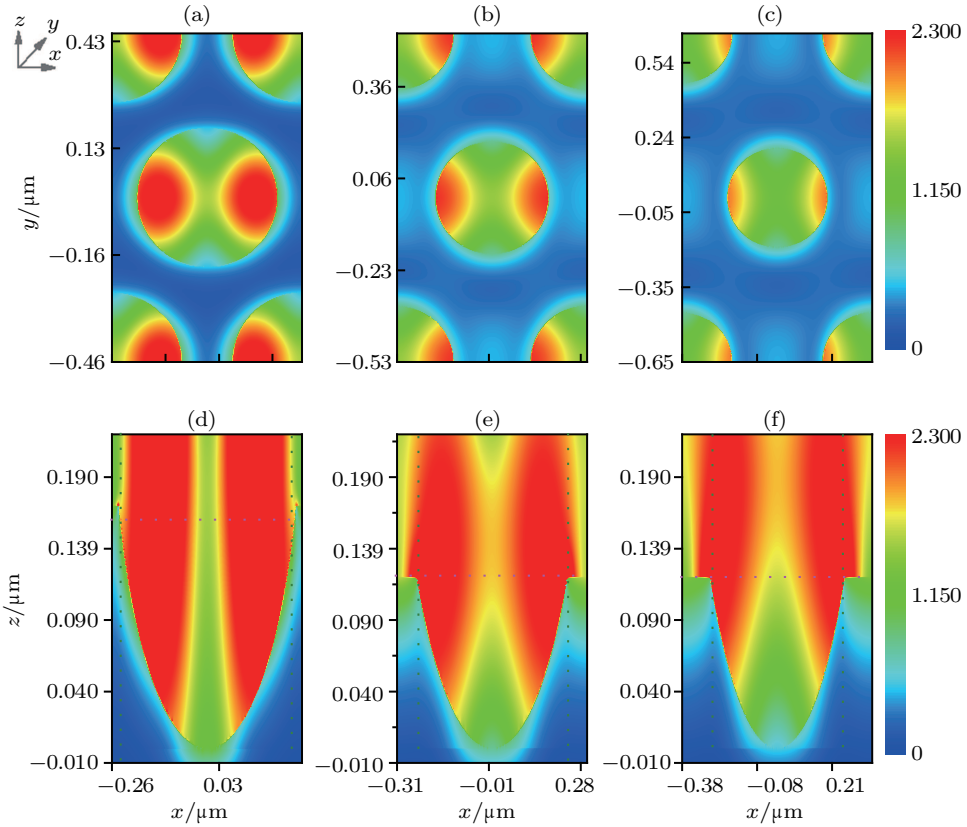


Fig. 6. (color online) Field amplitude distributions of dips R2 in spectra of samples S2 in the *xy*-plane (a)–(c) and *xz*-plane (d)–(f). The dashed lines show EF distributions in the voids.

As for MOKE with resonant spectrum, high intensity and sensitivity can be demonstrated. Besides the basic physical research and MO setups such as modulators and isolators, materials with resonant MOKE are urgent for optical biosensors.[66–71] The sensitivity can be extrapolated according to[55]

$$\begin{aligned} S &\propto \partial\theta_k/\partial\tilde{n}(\lambda) = (\partial\theta_k/\partial\lambda)(\partial\tilde{n}(\lambda)/\partial\lambda)^{-1} \\ &\propto \partial\varepsilon_k/\partial\tilde{n}(\lambda) = (\partial\varepsilon_k/\partial\lambda)(\partial\tilde{n}(\lambda)/\partial\lambda)^{-1}, \end{aligned} \tag{6}$$

where $\tilde{n}(\lambda)$ is the effective complex refractive index of the system, and $\partial\tilde{n}(\lambda)/\partial\lambda$ is proportional to $\partial R/\partial\lambda$.

Figure 7 shows derivative spectra versus λ of both polar MOKE (Figs. 7(a)–7(g)) and optical reflection (Figs. 7(h)–7(n)) of samples S1 (MOKE: Figs. 7(a)–7(d), reflectivity: Figs. 7(h)–7(k)) and samples S2 (MOKE: Figs. 7(e)–7(g), reflectivity: Figs. 7(l)–7(n)). In Figs. 7(a) and 7(d), the derivative spectra of θ_k and ε_k of samples S1 with deposition time $t = 20$ s and 150 s demonstrate a symmetry dip-peak shape, while, for those of the other two as indicated in Figs. 7(b) and 7(c) with $t = 60$ s and 100 s, the dip-peak shape spectra show an asymmetry characteristic. The derivation spectra of reflectivity in Figs. 7(h)–7(k) of samples S1 demonstrate the same tendency, the corresponded derivation spectra of reflectivity in Figs. 7(h) and 7(k) reveal symmetry attributions, with $\partial\theta_k/\partial\lambda = 0$ at the resonant point, but these are hardly discerned in Figs. 7(i) and 7(j). High sensitivity can be clearly seen for samples with deposition $t = 20$ s (Figs. 7(a) and 7(h)) and 150 s (Figs. 7(d) and 7(k)). In Fig. 7(a), at resonant point, $\partial\varepsilon_k/\partial\lambda$ is negative maximum, and in Fig. 7(h), $\partial R/\partial\lambda = 0$ which makes $S \to \infty$. From Figs. 7(d) and 7(k), we read $\partial\theta_k/\partial\lambda \to$ maximum at the point where $\partial R/\partial\lambda = 0$, which also results in $S \to \infty$. Besides the sensitivity, the intensity and half bandwidth are also important parameters to deliver the performance of devices. For resonant MOKE induced by the plasma edge in Fig. 3(a), the bandwidth is narrower about 15 nm, but the intensity is less than 0.1°. However, resonant MOKE induced by surface lattice plasma in Fig. 3(d) reveals high intensity but broader half bandwidth due to the high absorption of ferromagnetic materials.

Evidently, the MOKE spectra of samples S2 with $a =$ 530 nm and 620 nm in Figs. 4(a) and 4(b) demonstrate higher and narrower aspects, the magnitude is larger than 1°, and the half-height bandwidth is less than 15 nm. High sensitivity could also be revealed for the sample with lattice $a = 530$ nm in Figs. 7(e) and 7(l), where at the resonant point, $\partial\varepsilon_k/\partial\lambda$ (Fig. 7(e)) has a negative maximum and $\partial R/\partial\lambda = 0$ (Fig. 7(l)). Though high intensity and a narrow bandwidth are also revealed in the MOKE derivative spectrum of the sample with lattice $a = 620$ nm (Fig. 7(f)), the sensitivity might be lowered due to the slight deviation of $\partial R/\partial\lambda$ from zero at resonant point. With further increasing the lattice $a = 760$ nm, broad and lower $\partial\varepsilon_k/\partial\lambda$ (the red line) appears in Fig. 7(g), the $\partial R/\partial\lambda$ nearly approaches to the highest value in Fig. 7(n), further lowered sensitivity appears in consequence.

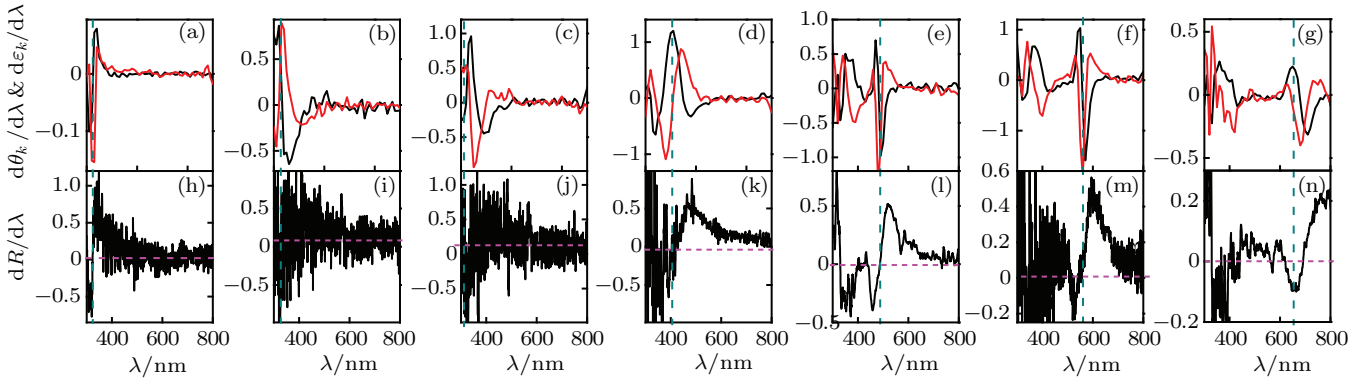


Fig. 7. (color online) $\partial\theta_k/\partial\lambda$ (black lines) and $\partial\varepsilon_k/\partial\lambda$ (red lines) (a)–(g) and $\partial R/\partial\lambda$ (h)–(n) as a function of λ for samples S1 and S2. The dashed dark green lines indicate the resonance locations.

4. Conclusion and perspectives

With the aid of nanosphere lithography and electrochemical deposition, ferromagnetic Co nanovoids arrayed on noble metal surface were fabricated. The polar magneto–optical Kerr effects showed a resonance-like shape. Combined with the AFM image and reflectivity spectra, we ascribed those resonant PMOKEs to the bulk Ag plasma edge, void plasmon (nanocavity) resonance, and surface lattice resonance, respectively. The simulated EF distribution analysis consolidated the physical mechanism of those optical modes induced by different aspect ratios of ferromagnetic voids, which is different from our former work where MOKE is modulated by Mie scattering,[58] or by guide mode,[54] with the introduction of the PSS array. Here, the resonant polar MOKE induced by void plasmons (nanocavity) possesses high optical sensitivity, high intensity, and a narrow bandwidth at resonant location, which would facilitate the fabrication of optical biosensors, ultra-compact optical modulators, isolators, and other nonreciprocal devices.

Acknowledgment

We thank the support of Soft-X Ray Interference Lithography Beam line (BL08U1B) in SSRF for sample preparation and characterization.

References

[1] Alù A, Fleury R and Sounas D 2014 *IEEE Photonics Conference*, October, 12–16, 2014, San Diego, CA, USA
[2] Khanikaev A B, Mousavi S H, Shvets G and Kivshar Y S 2010 *Phys. Rev. Lett.* **105** 126804
[3] Fotue A J, Issofa N, Tiotsop M, Kenfack S C, Tabue D M P, Wirngo A V, Fotsin H and Fai L C 2016 *Superlatt. Microstruct.* **90** 20
[4] Düchs G, Rikken G L J A, Grenet T and Wyder P 2001 *Phys. Rev. Lett.* **87** 127402
[5] Lax B and Wright G 1960 *Phys. Rev. Lett.* **4** 16
[6] Fan S 2010 *Nat. Photon.* **4** 76
[7] Clavero C, Yang K, Skuza J R and Lukaszew R A 2010 *Opt. Express* **18** 7743
[8] Armelles G, Caballero B, Prieto P, Garcia F, Cebollada A, Gonzalez M U and Garcia-Martin A 2014 *Nanoscale* **6** 3737
[9] Liu M and Zhang X 2013 *Nat. Photon.* **7** 429
[10] Chin J Y, Steinle T, Wehlus T, Dregely D, Weiss T, Belotelov V I, Stritzker B and Giessen H 2013 *Nat. Commun.* **4** 1599
[11] Belotelov V I, Akimov I A, Pohl M, Kotov V A, Kasture S, Vengurlekar A S, Gopal A V, Yakovlev D R, Zvezdin A K and Bayer M 2011 *Nat. Nano* **6** 370
[12] Yao X, Tokman M and Belyanin A 2015 *Opt. Express* **23** 795
[13] Hopkins B, Filonov D S, Miroshnichenko A E, Monticone F, Alù A and Kivshar Y S 2015 *ACS Photon.* **2** 724
[14] Reim W and Schoenes J 1990 *Magneto-Optical Spectroscopy of F-electron Systems* (Chapter 2) (France: Elsevier Science Publishers) pp. 135–157
[15] Temnov V V, Armelles G, Woggon U, Guzatov D, Cebollada A, Garcia-Martin A, Garcia-Martin J M, Thomay T, Leitenstorfer A and Bratschitsch R 2010 *Nat. Photon.* **4** 107
[16] Brion J J, Wallis R F, Hartstein A and Burstein E 1972 *Phys. Rev. Lett.* **28** 1455
[17] Feil H and Haas C 1987 *Phys. Rev. Lett.* **58** 65
[18] Katayama T, Suzuki Y, Awano H, Nishihara Y and Koshizuka N 1988 *Phys. Rev. Lett.* **60** 1426
[19] De A and Puri A 2002 *J. Appl. Phys.* **91** 9777
[20] Fumagalli P, Spaeth C, Rudiger U and Gambino R J 1995 *IEEE Trans. Magn.* **31** 3319
[21] Pendry J B, Martin-Moreno L and Garcia-Vidal F J 2004 *Science* **305** 847
[22] Hibbins A P, Evans B R and Sambles J R 2005 *Science* **308** 670
[23] Schuller J A, Barnard E S, Cai W, Jun Y C, White J S and Brongersma M L 2010 *Nat. Mater.* **9** 193
[24] Armelles G, Cebollada A, García-Martín A, González M U, García F, Meneses-Rodríguez D, de Sousa N and Froufe-Pérez L S 2013 *Opt. Express* **21** 27356
[25] Pohl M, Kreilkamp L E, Belotelov V I, Akimov I A, Kalish A N, Khokhlov N E, Yallapragada V J, Gopal A V, Nur-E-Alam M, Vasiliev M, Yakovlev D R, Alameh K, Zvezdin A K and Bayer M 2013 *New J. Phys.* **15** 075024
[26] Kostylev N, Maksymov I S, Adeyeye A O, Samarin S, Kostylev M and Williams J F 2013 *Appl. Phys. Lett.* **102** 121907
[27] Wang L, Clavero C, Huba Z, Carroll K J, Carpenter E E, Gu D and Lukaszew R A 2011 *Nano Lett.* **11** 1237
[28] Kalska-Szostko B, Hilgendorff M, Giersig M and Fumagalli P 2013 *Appl. Phys. A* **111** 853
[29] Armelles G, González-Díaz J B, García-Martín A, García-Martín J M, Cebollada A, González M U, Acimovic S, Cesario J, Quidant R and Badenes G 2008 *Opt. Express* **16** 16104
[30] González-Díaz J B, García-Martín A, García-Martín J M, Cebollada A, Armelles G, Sepúlveda B, Alaverdyan Y and Käll M 2008 *Small* **4** 202
[31] Torrado J F, González-Díaz J B, González M U, García-Martín A and Armelles G 2010 *Opt. Express* **18** 15635
[32] Kekesi R, Martín-Becerra D, Meneses-Rodríguez D, García-Pérez F, Cebollada A and Armelles G 2015 *Opt. Express* **23** 8128
[33] Atmatzakis E, Papasimakis N, Fedotov V A and Zheludev N I 2014 *CLEO*: 2014, *OSA Technical Digest (online)* p. STu1H.6
[34] Valente J A, Ou J Y, Plum E, Youngs I J and Zheludev N I *CLEO*: 2014, *OSA Technical Digest (online)* p. FM4C.3

[35] Luo X, Zhou M, Liu J, Qiu T and Yu Z 2016 *Appl. Phys. Lett.* **108** 131104

[36] Floess D, Chin J Y, Kawatani A, Dregely D, Habermeier H U, Weiss T and Giessen H 2015 *Light Sci. Appl.* **4** e284

[37] Fang K, Yu Z and Fan S 2012 *Nat. Photon.* **6** 782

[38] Estep N A, Sounas D L, Soric J and Alù A 2014 *Nat. Phys.* **10** 923

[39] Chang L, Jiang X, Hua S, Yang C, Wen J, Jiang L, Li G, Wang G and Xiao M 2014 *Nat. Photon.* **8** 524

[40] Ochiai T 2015 *Sci. Technol. Adv. Mater.* **16** 014401

[41] Okada K N, Takahashi Y, Mogi M, Yoshimi R, Tsukazaki A, Takahashi K S, Ogawa N, Kawasaki M and Tokura Y 2016 *Nat. Commun.* **7** 12245

[42] Ken N, Okada Y T, Masataka M, Ryutaro Y, Atsushi T, Kei S Takahashi, Naoki O, Masashi K and Yoshinori T 2016 ArXiv: 1603.02113

[43] Crassee I, Levallois J, Walter A L, Ostler M, Bostwick A, Rotenberg E, Seyller T, van der Marel D and Kuzmenko A B 2010 *Nat. Phys.* **7** 48

[44] Shimano R, Yumoto G, Yoo J Y, Matsunaga R, Tanabe S, Hibino H, Morimoto T and Aoki H 2013 *Nat. Commun.* **4** 1841

[45] Aivazian G, Gong Z, Jones A M, Chu R L, Yan J, Mandrus D G, Zhang C, Cobden D, Yao W and Xu X 2015 *Nat. Phys.* **11** 148

[46] Wallis R F, Brion J J, Burstein E and Hartstein A 1974 *Phys. Rev. B* **9** 3424

[47] Zharov A A and Kurin V V 2007 *J. Appl. Phys.* **102** 123514

[48] Ctistis G, Papaioannou E, Patoka P, Gutek J, Fumagalli P and Giersig M 2009 *Nano Lett.* **9** 1

[49] Chen T and Lu X H 2015 *Chin. Phys. Lett.* **32** 024204

[50] Maccaferri N, Gonzalez-Diaz J B, Bonetti S, Berger A, Kataja M, van Dijken S, Nogues J, Bonanni V, Pirzadeh Z, Dmitriev A, Akerman J and Vavassori P 2013 *Opt. Express* **21** 9875

[51] Maccaferri N, Berger A, Bonetti S, Bonanni V, Kataja M, Qin Q H, van Dijken S, Pirzadeh Z, Dmitriev A, Nogués J, Åkerman J and Vavassori P 2013 *Phys. Rev. Lett.* **111** 167401

[52] Kataja M, Hakala T K, Julku A, Huttunen M J, van Dijken S and Torma P 2015 *Nat. Commun.* **6** 7072

[53] Chen L Y, Tang Z X, Gao J L, Li D Y, Lei C X, Cheng Z Z, Tang S L and Du Y W 2016 *Chin. Phys. B* **25** 113301

[54] Zhang X, Shi L, Li J, Xia Y J, Shi Z, Zi J and Zhou S M 2012 *J. Phys. D: Appl. Phys.* **45** 405002

[55] Zhang X, Shi L, Li J, Xia Y J, Shi Z and Zhou S M 2013 *Chin. Phys. B* **22** 117803

[56] Zhang X, Shi L, Li J, Xia Y J, Shi Z and Zhou S M 2013 *Chin. Phys. Lett.* **30** 37801

[57] He P, Zhang X, Shi L, Li J and Zhou S 2012 *Appl. Opt.* **51** 5713

[58] Liu Z, Shi L, Shi Z, Liu X H, Zi J, Zhou S M, Wei S J, Li J, Zhang X and Xia Y J 2009 *Appl. Phys. Lett.* **95** 032502

[59] Zvezdin A K and Kotov V A 1997 *Modern Magnetooptics and Magnetooptical Materials* (London: IOP Publishing Ltd) p. 101

[60] Huber E E M 1988 *Appl. Phys. A* **47** 131

[61] Wheeler H A and Fellow I R E 1942 *Proceedings of the I.R.E.* **30** 412

[62] Teperik T V, Popov V V, de Abajo F J G, Abdelsalam M, Bartlett P N, Kelf T A, Sugawara Y and Baumberg J J 2006 *Opt. Express* **14** 1965

[63] Cole R M, Baumberg J J, de Abajo F J G, Mahajan S, Abdelsalam M and Bartlett P N 2007 *Nano Lett.* **7** 2094

[64] Fox M 2001 *Optical Properties of Solids* (New York: Oxford University Press)

[65] Ebbesen T W, Lezec H J, Ghaemi H F, Thio T and Wolff P A 1998 *Nature* **391** 667

[66] Pistora J, Lesnak M, Vlasin O and Cada M 2010 *Opt. Appl.* **40** 883

[67] Kämpf K, Kübler S, Wilhelm H F and Ehresmann A 2012 *J. Appl. Phys.* **112** 034505

[68] Manera M G, Ferreiro-Vila E, Garcia-Martin J M, Garcia-Martin A and Rella R 2014 *Biosens. Bioelectron.* **58** 114

[69] Huang H T, Chen P J, Ger T R, Chi Y J, Huang C W, Liao K T, Lai J Y, Chen J Y, Peng W Y, Zhang Q, Hsieh T F, Sheu W J and Wei Z H 2014 *IEEE Trans. Magn.* **50** 1001604

[70] Maccaferri N, E Gregorczyk K, de Oliveira T V A G, Kataja M, van Dijken S, Pirzadeh Z, Dmitriev A, Åkerman J, Knez M and Vavassori P 2015 *Nat. Commun.* **6** 6150

[71] Ignatyeva D O, Knyazev G A, Kapralov P O, Dietler G, Sekatskii S K and Belotelov V I 2016 *Sci. Rep.* **6** 28077